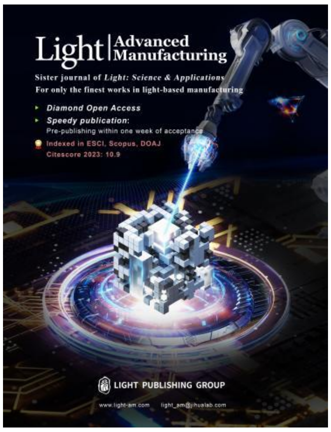

Nanoscale characterization of stress in Si nanowires for semiconductor qubit fabrication

Gin´es Gonz´alez-Guirado, Vanessa Hinojosa-Chasi-quiza, Juli´an Anaya, Jordi Antoja-Lleonart, Jordi Llobet, Alberto del Moral, Albert Guerrero, Olga Muntada, Teresa Elenes-Cervantes, Joan Bausells, Juan Jim´enez, Jorge Souto, Francesc P´erez-Murano, Jose Luis Pura

Cite this article as: Gin´es Gonz´alez-Guirado, Vanessa Hinojosa-Chasiquiza, Juli´an Anaya, Jordi Antoja-Lleonart, Jordi Llobet, Alberto del Moral, Albert Guerrero, Olga Muntada, Teresa Elenes-Cervantes, Joan Bausells, Juan Jim´enez, Jorge Souto, Francesc P´erez-Murano, Jose Luis Pura. Nanoscale characterization of stress in Si nanowires for semiconductor qubit fabrication. *Light: Advanced Manufacturing* accepted article preview 17 July, 2026; doi: 10.37188/lam.2026.124

Received 24 February 2026; Revised 12 May 2026; Accepted 2 June 2026;
Accepted article preview online 17 July 2026

Nanoscale characterization of stress in Si nanowires for semiconductor qubit fabrication

Ginés González-Guirado[1], Vanessa Hinojosa-Chasiquiza[1], Julián Anaya[1], Jordi Antoja-Lleonart[2], Jordi Llobet[2], Alberto del Moral[2], Albert Guerrero[2], Olga Muntada[2], Teresa Elenes-Cervantes[2], Joan Bausells[2], Juan Jiménez[1], Jorge Souto[1], Francesc Pérez-Murano[2], and Jose Luis Pura[1,*]

[1] *GdS Optronlab, Ed. LUCIA, Paseo de Belén 19, Universidad de Valladolid, 47011 Valladolid, Spain*

[2] *IMB-CNM (CSIC), Campus UAB, Bellaterra 08193, Barcelona, Spain*

[*] Correspondence to Jose Luis Pura: joseluis.pura@uva.es

Abstract

The advancement of quantum computing technologies requires the scalable development of reliable qubit platforms. One promising strategy to address this challenge involves adapting current silicon nanoelectronic technology to meet the requirements for semiconductor-based qubits. In this context, Si nanowires (NWs) are particularly attractive for realizing spin-based qubits in fully depleted silicon on insulator (FD-SOI) platforms. The performance of quantum devices is critically dependent on the quality of the materials, including crystalline disorder or processing-induced modifications. We report here a μ-Raman spectroscopy investigation of Si NWs fabricated by dry etching for qubit fabrication. To determine the structural quality of the processed NWs and the presence of stress, we present two different methodologies. First, intentionally localized laser heating of the NW permits us to decouple the Raman signals of the Si NW and the substrate to extract the NW stress. Second, the removal of the Si substrate beneath certain NWs allows for a direct measurement of the free-standing Si NW stress. These experimental measurements are supported by Finite Element Methods simulations to analyze the stress profiles correctly. We obtained comparable stress values with both methodologies within the range of 0.17-0.34 GPa, corresponding to small elastic strains (0.1-0.2%) that would lift the heavy-hole/light-hole degeneracy and reduce band mixing. These modifications could favor hole-qubit operation while remaining well below mechanical stability thresholds. The results confirm the suitability of the etching process for fabricating Si NW-based qubits and establish a reliable platform for a robust non-invasive characterization, even under unfavorable experimental conditions.

Keywords: Silicon Nanowires, Semiconductor Qubits, Micro-Raman Spectroscopy, Stress Engineering, Dry Etching, Spin-Based qubits.

Introduction

In recent years, research in quantum computing and quantum technologies has grown substantially, driving significant advances in both hardware design and algorithm development [1]. Despite the huge advances in the field, the currently available quantum processors barely reach the threshold of a thousand physical qubits, a number that is still insufficient to solve complex problems and span general applications. According to Fowler et al. [2], thousands of logical qubits, and thus millions of physical qubits, are necessary for certain algorithms when quantum error correction is applied to ensure reliable outcomes. New error-correcting codes and architectures are emerging every day, improving the ratio of logical to physical qubits and lowering the hardware requirements. Even so, reaching the scale of thousands of logical qubits is expected to require at least 10^5 physical qubits [3]. Therefore, the advancement of quantum computing technologies requires the scalable development of reliable qubit platforms. One of the most promising strategies to address this challenge is the adaptation of the mature Complementary Metal-Oxide Semiconductor (CMOS) technology for fabricating semiconductor-based qubits. In this context, Si nanowires (NWs), which provide strong lateral electron confinement in two dimensions, are particularly attractive platforms for realizing spin-based qubits [4]. The use of isotopically enriched ^{28}Si has enabled exceptionally long spin coherence times for both nuclear and electron spins [5, 6, 7]. Beyond this, NWs offer high carrier mobility, bandgap tunability, and compatibility with current device fabrication technologies. From a scalability perspective, NWs offer a clear advantage: they enable the integration of multiple local metallic or superconducting contacts and electrostatic gates on the top, bottom, and sides of the wire, providing a precise 3D control of electrons via spin–orbit and electrostatic interactions [8, 9, 10, 11].

The performance of electronic devices is highly dependent on the quality of the materials.

This dependence becomes even more dramatic for quantum devices that critically rely on the sustainment of quantum coherence. Factors such as the presence of crystalline disorder, the surface condition, and modifications introduced during device processing significantly impact their performance and reliability [12, 13, 14]. Given the precision required during the manufacturing process for proper qubit function, it is essential to employ characterization techniques capable of detecting structural defects at the micro- and nanoscales. The characterization methods must be non-destructive, enabling in situ evaluation of devices during fabrication without introducing damage. μ-Raman spectroscopy meets these criteria due to its non-invasive character and its exceptional sensitivity to structural properties, capable of resolving subtle variations in material properties such as the presence of defects, surface states [15], residual stress [16], and thermal effects [17].

Despite their subwavelength diameter, Si NWs can be effectively characterized by μ-Raman spectroscopy due to polarization-dependent resonance effects when the incident electric field is aligned parallel to the NW axis [18, 19]. Under these conditions, the NW behaves as an optical dipolar nanoantenna, maximizing the internal electric field and, consequently, the Raman scattering efficiency. In contrast, when the polarization is perpendicular to the axis, the internal field is significantly attenuated, leading to a much weaker response [20]. The magnitude of this enhancement is further governed by the NW diameter, the excitation wavelength, and the substrate. In particular, for a 532 nm excitation wavelength, Si NWs with diameters in the 40–60 nm range exhibit stronger resonant enhancement than thicker NWs (60–80 nm) [18, 21]. Therefore, selecting an appropriate excitation wavelength relative to the NW dimensions and environment is essential for optimizing the Raman signal.

This polarization-dependent response has been an essential tool for probing the physical properties of one-dimensional nanostructures, including crystallographic orientation and optical selection rules [22, 23]. In particular, such effects have been utilized to evaluate local strain distributions and mechanical stress in nanoscale semiconductor systems, as the antenna-enhanced signal provides the precision required to resolve subtle phonon frequency shifts [24, 25]. Consequently, μ-Raman spectroscopy provides a robust nanoscale characterization technique with enhanced detection capability for investigating the structural and mechanical properties of anisotropic nanostructures.

Residual stress is known to play a key role in Si nanodevices, often leading to buckling or curvature if they are released [26]. Also, even modest residual stress can lift the heavy-hole/light-hole degeneracy and reduce band mixing, which could enhance hole-qubit operation while remaining well below mechanical damage thresholds [27, 28, 29]. In this work, we report a μ-Raman investigation of Si NWs to determine their structural quality and stress. The studied Si NWs have been fabricated by dry etching on silicon-on-insulator (SOI) wafers using a combined mix-and-match optical/e-beam lithography approach. We present two different accurate stress extraction methodologies: first, intentional localized laser heating of the NW, and second, the removal of both the underlying bulk Si substrate and the buried oxide (BOX) SiO_2 layer to obtain free-standing Si NWs. Both approaches provided reliable and equivalent measurements of the stress. At the same time, simulations based on Finite Element Methods (FEM) were performed to properly understand the experimental results and extract additional information about the stress distributions in the NWs.

Sample Description

Si NWs were fabricated by dry etching on silicon-on-insulator (SOI) wafers. Figure 1 (a) shows the scheme of the samples, which consist of a boron-doped monocrystalline Si substrate oriented along the $\langle 001 \rangle$ direction with a thickness of 725 µm, a 400 nm thermal SiO_2 layer, and a 50 nm monocrystalline Si layer, also oriented along $\langle 001 \rangle$. The NWs and their source/drain connections were defined on this top Si layer using a mix-and-match lithography approach combining electron-beam and optical patterning, followed by dry etching. The NWs widths range from 40 to 60 nm, and the width of the NW shown in Figure 1 (b) is 50 nm. The NWs analyzed by Raman spectroscopy for stress extraction were 50 nm wide. The geometrical parameters used as input for the FEM simulations are illustrated in Figure 1 (a).

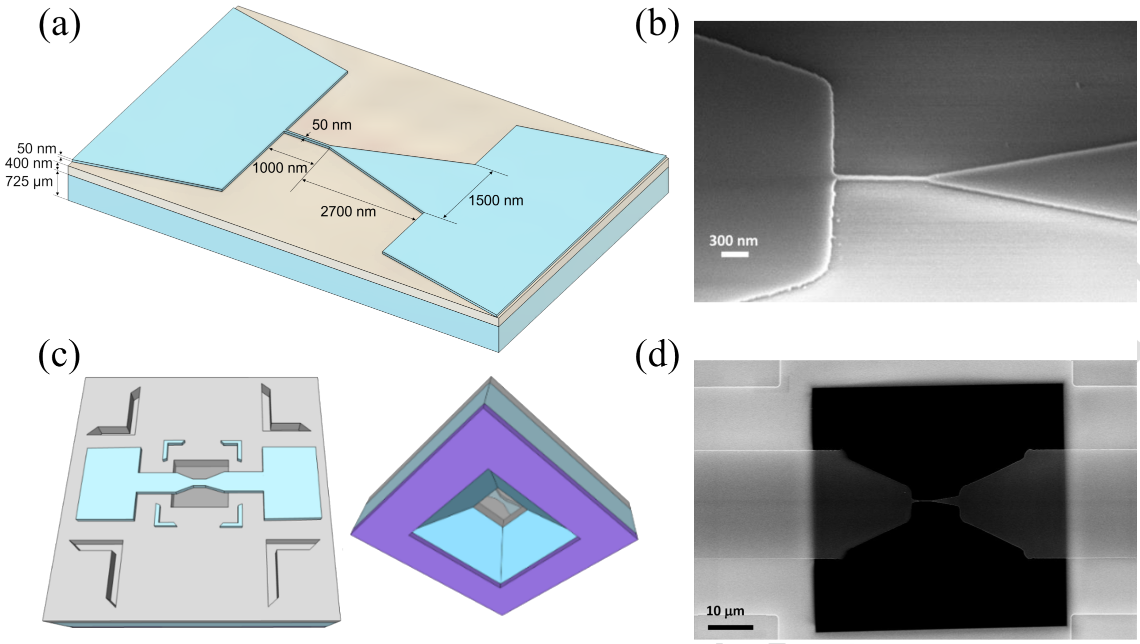

Figure 1: (a) Schematic representation of the sample. (b) SEM image of a Si NW and its pads. (c) Illustration of the free-standing NW, presented in both top and bottom views. (d) SEM image of a free-standing NW, suspended over the etched window and supported only by the electrodes on the surrounding frame.

To access the Si NW information directly, in some of the samples we removed the Si substrate beneath the NWs in a controlled manner using optical lithography and anisotropic etching in the back side of the wafer. The wafer-scale local Si substrate removal takes place after the NWs fabrication process. The samples were prepared by depositing a SiN_x mask, and subsequently, an anisotropic KOH etching removed the Si substrate beneath the NW, avoiding damage to the NW. The oxide layer directly beneath the Si NWs was selectively removed by an HF bath, resulting in free-standing NWs, while the oxide in the surrounding frame regions of the sample remained intact. A schematic representation of the result is presented in Figure 1 (c). The NWs retained their integrity after subsequent dicing and cleaning steps, as shown in the SEM image in Figure 1 (d). See Materials and methods for further details of the sample's fabrication process.

Results and Discussion

The characterization of Si NWs etched on SOI wafers is particularly challenging due to the combination of reduced signal strength and intertwined physical effects. The nanoscale diameter of the NWs leads to a very small scattering volume, so that the Raman response is typically dominated by the underlying Si substrate because the optical penetration depth exceeds the NW thickness. At the same time, the interpretation and isolation of the NW contribution is complicated by the coexistence of several mechanisms affecting the Raman peak position and linewidth, including residual stress, laser-induced heating, and eventually phonon confinement [30, 31]. In particular, it is well established that even moderate excitation powers can induce significant local heating in Si nanowires, producing redshifts and broadenings comparable to or larger than those expected from confinement or strain, which can easily lead to misinterpretation of the spectra [32, 33]. Moreover, thermal effects are exacerbated by the reduced thermal conductivity of nanoscale Si, dominated by surface and boundary scattering, which limits heat dissipation and promotes non-uniform temperature distributions. Also, the SOI configuration further increases the characterization complexity, as the buried oxide modifies both heat transport and mechanical boundary conditions, introducing additional stress components through interfacial strain transfer and thermal mismatch [31]. These challenges are consistent with broader analyses of SOI fabrication and characterization, which highlight the intrinsic difficulty of obtaining quantitative, layer-specific stress values in ultrathin Si films [34, 35].

Even though routine methodologies are applied to mitigate background signals, e.g. low incident laser power or pinhole control for limiting the depth of field, the NW geometry and SOI structure allow the incident laser beam to reach the Si substrate. Other possible approaches, like using UV excitation to leverage its shallow penetration depth, still result in substrate illumination as the beam is able to circumvent the NW diameter. In addition, the low stress values typically fall within the measurement error range, further complicating an accurate estimation of this magnitude.

Altogether, these factors make the reliable extraction of intrinsic NW properties from Raman measurements highly non-trivial and thus require carefully designed experimental strategies to decouple the different contributions. In order to overcome these challenges, two different approaches have been considered to characterize the NWs with sub-micron resolution.

In the first approach, we intentionally induced local heating of the NW with the incident laser beam to purposely modify the Raman spectrum of the NW and distinguish it from the signal of the unperturbed Si substrate beneath the NW. This allowed us to perform a two-peak fitting and extract information concerning only the NW. The main challenge of this approach is the modification of the NW Raman spectrum by the change in temperature. Thus, to obtain the stress on the NWs following this experimental approach, we must separate the thermal and stress contributions to the Raman peak shape.

In contrast, in the second method, we propose an alternative path to directly access the information of the Si NW by locally removing the underlying Si substrate using optical lithography and anisotropic etching, providing a benchmark against the laser-heating approach. By doing this, the absence of the underlying substrate permits a cleaner measurement of the Si NW.

Intentional localized laser heating

In order to differentiate the NW signal from that of the substrate, we induced intentional localized laser heating on the NW by applying a high enough excitation power. This modifies the NW Raman spectrum without causing damage and allows us to decouple the signal arising from the NW and the one coming from the Si substrate. The dissipation of heat in the NWs depends on the materials in their vicinity [36], their dimensions [21], and their surface roughness [37]. In this case, the NWs lie on SiO_2, which has very low thermal conductivity as compared to bulk Si. Furthermore, the thermal conductivity of the NW decreases with its diameter [38]; also, the surface roughness can be significant as a result of the etching process, which can further reduce the thermal conductivity by enhancing diffusing phonon scattering [39, 40, 41]. Hence, the heat dissipation capability of the NWs is significantly reduced with respect to bulk Si.

When the NW is heated by the laser beam, the temperature-induced changes in phonon frequency and linewidth must be considered to obtain the real stress on the NW. The temperature dependence of the phonon frequency can be expressed as [42]:

$$\omega(T) = \omega_0 + \Delta\omega_{te}(T) + \Delta\omega_{anhar}(T) \tag{1}$$

where ω_0 is the phonon frequency at 0 K, $\Delta\omega_{te}$ is the Raman shift due to thermal expansion, and $\Delta\omega_{anhar}$ is due to anharmonic phonon decay (phonon-phonon coupling). The thermal expansion term is described by the following equation [42]:

$$\Delta\omega_{te}(T) = \omega_0 \left(\exp\left[-3\gamma \int_0^T \alpha(T')dT' \right] - 1 \right) \tag{2}$$

where $\alpha(T)$ is the coefficient of linear thermal expansion, $\gamma = 1.02$ is the Grüneisen parameter, and the integral is defined from 0 K to T, the temperature reached by the NW.

The anharmonic contribution is mainly due to the three- and four-phonon decay processes, and it is expressed as [42, 32]:

$$\Delta\omega_{anhar}(T) = A_1 \left(1 + \frac{2}{e^{\hbar\omega_0/2k_BT} - 1} \right) + A_2 \left(1 + \frac{3}{e^{\hbar\omega_0/3k_BT} - 1} + \frac{3}{(e^{\hbar\omega_0/3k_BT} - 1)^2} \right) \tag{3}$$

The linewidth is also shaped by the anharmonic phonon decay according to the following dependence:

$$\Gamma(T) = \Gamma_0 + B_1 \left(1 + \frac{2}{e^{\hbar\omega_0/2k_BT} - 1} \right) + B_2 \left(1 + \frac{3}{e^{\hbar\omega_0/3k_BT} - 1} + \frac{3}{(e^{\hbar\omega_0/3k_BT} - 1)^2} \right) \tag{4}$$

where $A_1 = -2.5606$ cm^{-1}, $A_2 = -0.0998$ cm^{-1}, $B_1 = 1.4093$ cm^{-1}, and $B_2 = 0.0667$ cm^{-1} are the anharmonic parameters, $\Gamma_0 = 1.3$ cm^{-1} is the linewidth at 0 K, and ω_0 = 526.0746 cm^{-1}. These parameters were determined from the experimentally measured variation as a function of temperature of the Raman shift and linewidth of a released Si membrane (top-Si layer) obtained by locally removing the BOX and bulk Si (Figure 1 (c) and (d)). The sample temperature was externally regulated using a temperature-controlled stage (see Experimental setup), and a low laser power was applied to prevent laser-induced heating.

In addition to the influence of temperature on the Raman signal, the effect of stress must also be considered. Stress alters the Raman spectrum relative to an unstressed sample: tensile stress induces a shift of the phonon frequency to lower frequencies, while compressive stress shifts it to higher frequencies. In a NW, which can be treated as a one-dimensional structure, only uniaxial stress along its axis should be considered, as the transverse in-plane components (σ_{yy} and σ_{zz}) relax, leaving the longitudinal component (σ_{xx}) alone.

Following [33, 43], the phonon frequency can be converted into the total stress using a linear relation derived from the phonon deformation potential formalism for Si. The stress shift coefficient (SSC) depends on the crystallographic orientation, stress configuration, and Raman selection rules. In this work, the SSC reported in [43] is used, yielding a value of -0.434 GPa/cm^{-1} for uniaxial stress along the $\langle 110 \rangle$ direction, considering a $\langle 001 \rangle$ surface and the present measurement configuration. This value is consistent with other reports in the literature. In particular, the work of Ureña et al. [44], carried out on top-down suspended Si NWs with a thickness of 200 nm fabricated along the $\langle 110 \rangle$ direction, subjected to uniaxial stresses up to 4.5 GPa and characterized using a 458 nm excitation wavelength, presents experimental conditions closely comparable to those of the present study and reports a SSC of -0.497 GPa/cm^{-1}. This result is in agreement with subsequent studies, such as [25] (15 nm Si NWs), with an SSC of approximately -0.526 GPa/cm^{-1}, and [45] (100 nm Si beams with doping) obtaining an SSC value of -0.395 GPa/cm^{-1}. Even though some of these works account for additional effects such as size-dependent elastic properties and doping, all the reported coefficients remain on the same tight range as the value used in this work. Under these assumptions, the stress is given by:

$$\sigma = -0.434 \left(\frac{\text{GPa}}{\text{cm}^{-1}} \right) \Delta\omega_s \tag{5}$$

To determine the stress distribution along the NW, we had to decouple the respective contributions of stress and temperature to the Raman shift. We assumed that the full width at half maximum (FWHM) depends solely on temperature, $\Gamma(T)$, since neither significant stress gradients nor structural disorder are present, and phonon confinement becomes relevant only for Si NWs with diameters below 20 nm [46, 47]. Thus, any change in FWHM can be attributed to temperature effects, allowing the temperature to be extracted from its variation using Eq. (4). In contrast, the phonon frequency depends on both stress and temperature, $\omega_{\text{exp}}(\sigma, T)$; therefore, once the temperature is determined from the FWHM, the temperature-induced Raman shift can be calculated, and the stress contribution to the frequency shift can be extracted.

After determining the temperature from the FWHM with Eq. (4), the corresponding temperature-induced Raman shift $\omega_{\text{temp}}(T)$ is calculated using Eq. (1). The thermal contribution is then given by $\Delta\omega_{\text{temp}}(T) = \omega_{\text{temp}}(T) - \omega_{\text{ref}}$, where $\omega_{\text{ref}} = 520.7$ cm^{-1} corresponds to the phonon frequency of unstressed Si at room temperature. The total experimental Raman shift relative to the Si reference is $\Delta\omega_{\text{exp}}(\sigma, T) = \omega_{\text{exp}}(\sigma, T) - \omega_{\text{ref}}$, which contains both thermal and stress contributions. Finally, subtracting the thermal component from the total shift yields the corrected Raman shift free of heating effects $\Delta\omega_{\text{NH}}(\sigma)$.

$$\Delta\omega_{\text{NH}}(\sigma) = \Delta\omega_{\text{exp}}(\sigma, T) - \Delta\omega_{\text{temp}}(T) \tag{6}$$

Now, $\Delta\omega_{\text{NH}}(\sigma)$ contains only the effect of stress, which allows us to directly extract it by using Eq. (5).

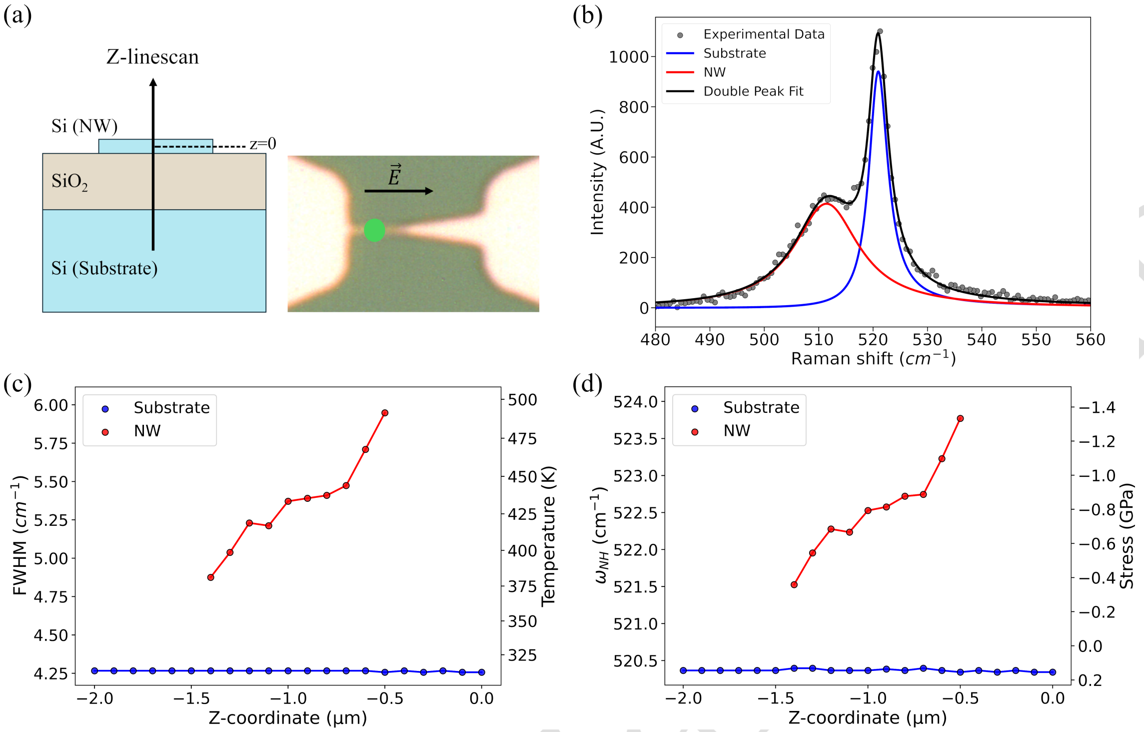

Figure 2: (a) Scheme of the z-linescan over the NW with the laser polarized parallel to the NW axis. $z = 0$ corresponds to the NW layer. (b) Representative Raman spectrum when the NW is locally heated with the excitation laser. Experimental data (points), double peak fit (black line), NW peak (red line), and substrate peak (blue line). (c) FWHM of the NW (red) and substrate (blue) Raman signals, together with the corresponding temperature (right y-axis), as a function of the z-coordinate along the linescan. (d) Raman shift of the NW (red) and substrate (blue) Raman signals, together with the corresponding stress (right y-axis), as a function of the z-coordinate along the linescan.

Using this procedure, we can obtain the stress in the Si NWs by performing in-depth Raman linescans, see Figure 2 (a). The representative Raman spectrum of a locally heated NW, is represented in Figure 2 (b). We can see that the Si peak on the NW shifts to lower frequencies and its FWHM increases due to the induced heating with respect to the substrate peak, which remains mostly unperturbed along the line-scan. For the fitting of the Raman spectra, we used a Lorentzian lineshape in the case of the NW and a Fano lineshape for the substrate peak [48]. The Fano lineshape was used because, at laser powers above 0.84 mW, which in terms of power density is $I \approx 2.06 \times 10^5$ W/cm^2, a slight Fano effect appears because of the photogenerated carriers. If the Fano effect is not considered, the temperature obtained from the FWHM (Eq. (4)) is overestimated.

In order to probe both the NW and the Si substrate, we performed multiple in-depth line scans, see Figure 2 (a), while increasing the laser power. To achieve confocality and reduce the Raman signal that comes from the substrate, we used the minimum pinhole size of the spectrometer (10 μm). By doing so, we reduced the Raman signal that arrives at the detector from planes apart from the focal plane. Thereby, we obtained the relative intensity between the peak of the NW and the peak of the substrate that allows us to deconvolute both peaks and obtain the stress on the NW.

Figure 2 (c) shows the FWHM and the corresponding temperature, calculated using Eq. (4), for the substrate (blue) and NW (red) peaks obtained from the double-peak fit, as a function of the line-scan depth (z-coordinate). We observed that above approximately 500 K, the Raman measurements no longer follow Eqs. (1–6) resulting in large errors in the stress calculations. This deviation from the behavior at lower temperatures may result from the significant temperature and stress gradients caused by the local laser heating at large temperatures, as the proposed treatment assumes homogeneous distributions of both. Defect formation and disorder have been ruled out since the low-temperature measurements can be reproduced after the high-power laser exposure. Taking this into account, we focus on the line-scan points where the NW peak temperature remains below 500 K, depicted in Figure 2 (c), to ensure the reliable determination of the intrinsic stress in the NW; full z-coordinate linescans are provided in the Supplementary Data, Figure S1. The corrected Raman shift without heating effects $\Delta\omega_{\mathrm{NH}}(\sigma)$ and its associated stress is shown in Figure 2 (d). The stress shown in this picture depends on the calculated temperature. The temperature dependence of stress originates from the differential response of the materials to laser heating: Si undergoes thermal expansion, while the SiO_2 remains mostly unaffected. As a result, the SiO_2 exerts a compressive stress (thermal stress) on the NW, which increases with temperature as the NW tends to expand further.

To determine the intrinsic stress of the NW, we represented the stress as a function of temperature and extrapolated the observed trends in the stress to room temperature (300 K). Hence, the compressive effect arising from the thermal expansion mismatch between the NW and SiO_2 is removed, yielding the intrinsic stress of the NW (marked by an X in Figure 3). This fitting is performed for different values of the incident laser power, showing a remarkable reproducibility. A stress value of 0.34 ± 0.04 GPa was obtained for NW 1 (Figure 3 (a)) and a stress value of 0.17 ± 0.04 GPa was obtained for NW 2 (Figure 3 (b)). These stress values correspond to minor elastic strains (0.1–0.2%) lying within the linear elastic regime of silicon [29, 49]. Strains of this magnitude are sufficient to break the cubic symmetry of the valence band and lift the heavy-hole (HH) and light-hole (LH) degeneracy via deformation-potential coupling, reducing HH–LH mixing even without quantum confinement [50, 28]. Such strain-induced valence-band splitting modifies hole spin–orbit coupling and the hole g-tensor, enabling reduced band mixing and access to operating regimes with lower sensitivity to electrical noise [51, 27, 52]. These effects are relevant for hole-based qubits, while the applied stress remains far below thresholds associated with defect formation or mechanical degradation.

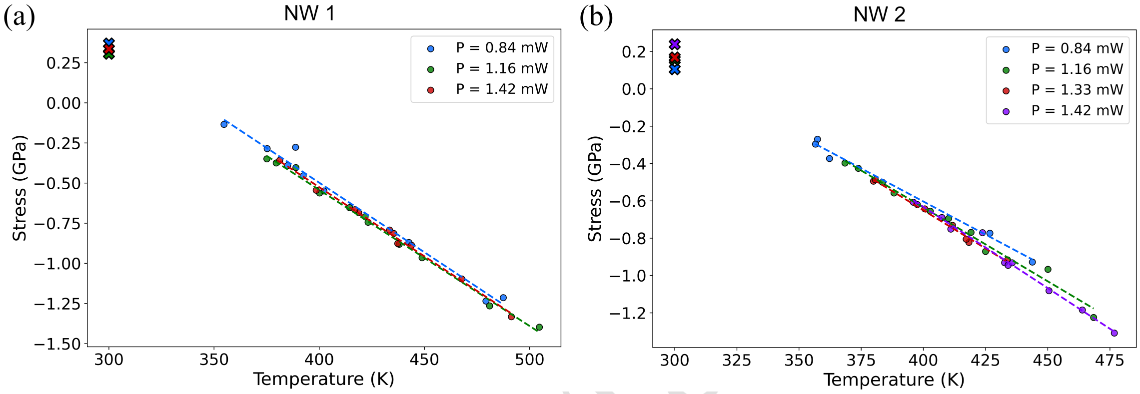

Figure 3: Stress as a function of temperature measured during the z-line scan at different laser powers. The intrinsic stress at 300 K, extracted for each laser power, is indicated by X markers for two different nanowires: (a) and (b).

Finally, it is important to note that the obtained data does not show any dependence on the applied laser power, as can be observed in the overlapping lines of Figure 3, which points to the robustness of the method and the intrinsic nature of the obtained room-temperature stress.

Characterization of free-standing Si NWs

An alternative path to directly accessing the information on the Si NWs consists of fabricating samples in which the Si substrate beneath the NW has been locally removed. However, the removal of the underlying Si and SiO_2 results in the partial relaxation of the, now, free-standing NW. As a result, the stress that we are measuring is not only the stress generated in the NW due to the etching process, but the stress due to the relaxation after removing the Si substrate and SiO_2 beneath the NW and the contact pads. This residual stress distribution originates from high-temperature processing followed by cooling to room temperature in SOI structures. It is mainly caused by the mismatch in the thermal expansion coefficients of Si and SiO_2. Upon cooling, Si tends to contract more than SiO_2, but this contraction is constrained by interfacial bonding, leading to tensile strain in the Si layer and compressive stress in the oxide [53, 54].

To determine the initial stress of the NW (prior to the substrate removal), a FEM simulation of the NW was carried out. The stress calculations were performed with the solid mechanics module of COMSOL Multiphysics. The geometrical parameters were obtained from the SEM measurements, detailed in Figure 1 (a). The top Si layer of SOI wafers is known to exhibit biaxial in-plane tensile stress [53]. However, after removal of the Si substrate and the SiO_2 layer beneath the NW and the pads, the mechanical boundary conditions are significantly modified, with the subsequent relaxation. The proposed FEM model contains only one free parameter, the initial NW stress (σ), while the sample geometry fully determines the remaining parameters. The simulation is run for σ in the range 0 - 1 GPa in steps of 0.05 GPa, yielding the measured stress after the Si substrate removal process. Then, the simulated stress profiles are extracted from the model results and fitted against the experimentally measured stress distribution. By doing this, the initial stress of the NW is uniquely determined by minimizing the deviation between the model and the experimental data.

To extract the stress distribution along the NW, an in-plane line scan was carried out. We used low laser power (P= 0.054 mW), which in terms of power density corresponds to $I = 1.33 \times 10^4$ W/cm^2, to avoid heating effects.

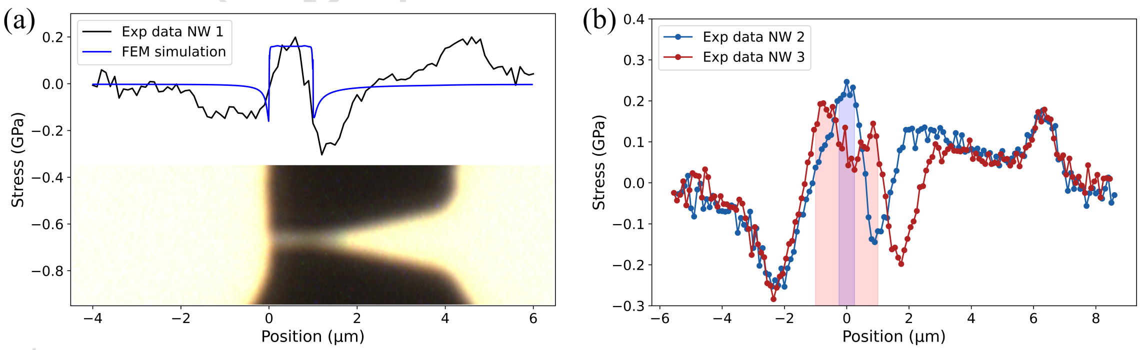

Figure 4: (a) Comparison of the experimental stress profile along the NW (black) with the FEM simulation stress results (blue). (b) Experimental stress profiles measured along two NWs of different lengths: NW 2 (500 nm, blue curve) and NW 3 (2000 nm, red curve). The regions corresponding to the NWs are shaded in blue for NW 2 and in red for NW 3.

Figure 4 (a) shows the in-plane stress obtained from the Raman measurements (black line) compared to the FEM simulations (blue line). The lower part of the figure illustrates an optical image of the NW along which the line scan was performed. The stress remains approximately constant and close to zero in the left pad, while a compressive stress of about −0.2 GPa develops at the junction with the NW. Along the NW, the stress gradually transitions to a tensile regime, reaching approximately 0.2 GPa. Upon approaching the junction with the tapered region, the stress becomes compressive again (around −0.3 GPa). At the onset of the tapered region, the structure relaxes once more. We can also notice the presence of a tensile stress in the central part of the tapered region, which appears on all the studied NWs (see Figure 4 (b)). Figure 4 (a) shows that the location of this tensile stress correlates with the end of the tapered region and its junction with the right pad. Thus, this tensile stress will most likely appear as a result of the different stiffness of these two regions and the corresponding local relaxation in this interface.

A good agreement is observed between the FEM simulations and the experimental data in the NW, which is the region of interest for producing the qubits.

Figure 4 (b) depicts the experimental stress profiles measured along two NWs of different lengths: NW 2 (500 nm, blue curve) and NW 3 (2000 nm, red curve). The stress distributions closely resemble the profile shown in Figure 4 (a), showing the same qualitative trends.

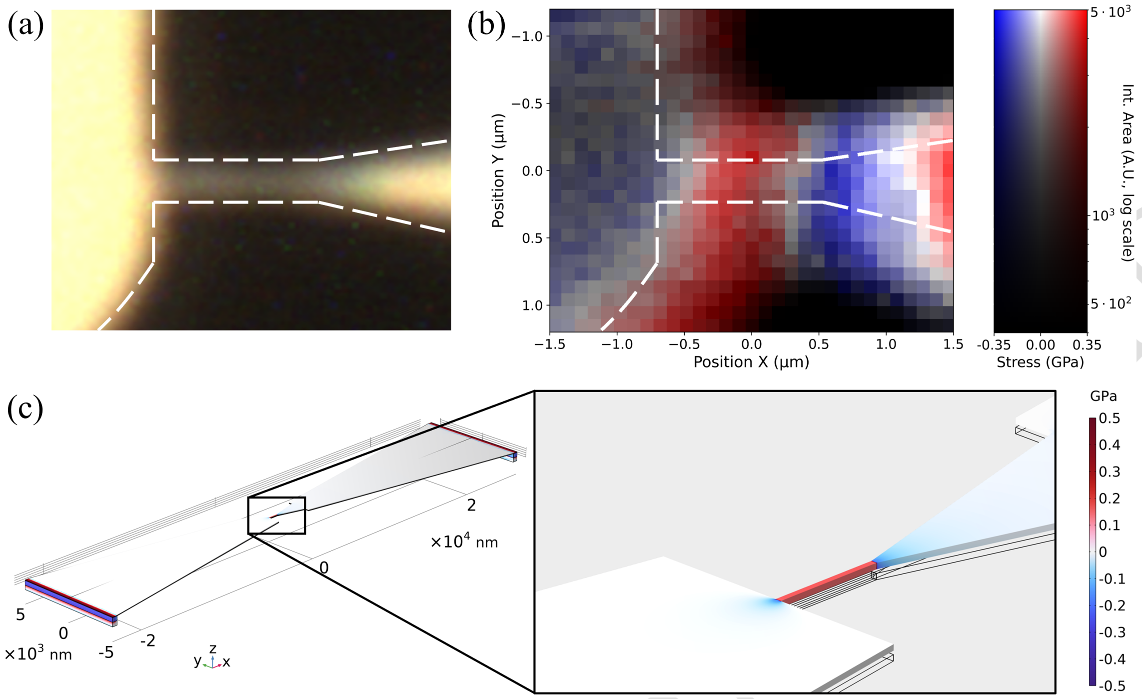

Figure 5: (a) Optical image of the region where the Raman spectral map was acquired for NW 1. (b) Experimental stress map corresponding to the optical image. The contour of the structure is drawn with white dashed lines. The intensity of the colorbar (vertical) represents the Raman integrated area on a logarithmic scale, while the color scale (horizontal) encodes the calculated stress in GPa: blue indicates compressive stress, white indicates zero stress, and red indicates tensile stress. (c) Structure and 3D stress distribution of the free-standing NW, the tapered region, and the pads obtained from the COMSOL model. On the right, a zoomed-in view of the NW highlights the local stress distribution. Note the slight bowing of the NW in the vertical direction as a result of the substrate removal. The black lines indicate the initial flat NW structure for reference and the deformation scale is 1:1.

In order to show the further capabilities of the proposed methodology, we performed 2D Raman mapping and calculated the corresponding stress distributions. Figures 5 (a) and (b) present an optical image and the experimental stress map obtained from the Raman mapping of NW 1, respectively. The outline of the structure is indicated by white dashed lines to aid in the interpretation of the stress map. The results are similar to those presented in Figure 4. A slight compressive stress (from ≈ -0.2 GPa) is observed at the junctions between the pads and the NW. Along the NW, the stress gradually evolves into a tensile regime, reaching approximately 0.2 GPa. In the tapered region, only a weak tensile stress is detected. In contrast, the edge of the tapered region shows a very slight compressive stress, likely influenced by the nearby junction between the NW and the tapered region. In addition, the stress at the edges, particularly along the edge of the left pad, exhibits a tensile character similar to that of the NW. Note that the signal detected beyond the physical edges of the sample (dashed white line) arises from the finite size of the laser spot. The beam is not point-like but has a diameter of ≈ 720 nm, and the measured Raman intensity therefore corresponds to the convolution of the Gaussian beam profile with the sample geometry.

Figure 5 (c) shows the structure and 3D stress distribution of the free-standing NW, the tapered region, and the pads obtained from the COMSOL model. At the ends of the pads, where the SiO_2 layer and the Si substrate remain intact, the Si experiences tensile stress, whereas the SiO_2 is under compressive stress. In contrast, the region of the NW and pads where both the SiO_2 and the Si substrate have been removed can relax. This relaxation leads to a partial release of stress and a slight bending of the structure toward the positive z-axis in our reference frame, as shown in the zoomed-in view on the right. Note that the structure formed by the black lines represents the initial state of the flat NW for comparison. The scale of the deformation is 1:1. This deformation induces additional stress within the NW and at its junctions with the pads. The NW experiences tensile stress, while compressive stress develops at its junctions with the pads, in good agreement with the experimental observations of Figure 4 and Figure 5 (b).

The obtained value of the initial stress that provides an optimum fit between the simulation and the experimental measurements is 0.21 ± 0.05 GPa, which is close to the values estimated with the previous method. The average stress for all the studied NWs is 0.21 ± 0.05 GPa, again within the values obtained in the Intentional localized laser heating section. Furthermore, according to the simulations, the initial stress in the NW can be obtained by scaling the measured stress after substrate removal by a factor of 1.33 (i.e., upon relaxation, the initial stress in the NW is reduced by 25%). This is a result of the linear relationship between the initial and measured stress values, as expected from the linear elastic model.

As a summary, it is worth mentioning that the first method is relatively straightforward in terms of measurements and sample preparation and maintains the non-destructive capabilities of Raman spectroscopy. These characteristics make it suitable for implementation in the production line. Its main drawback is the requirement for a more complex analysis like the one developed in this work. This methodology could be insufficient in situations in which the Si NWs are inaccessible, e.g., after the deposition of certain layers that prevent optical illumination, like metals for electrostatic gating. Also, it is important to note that the deposition of transparent layers like oxides does not limit its applicability. On the other hand, the second method is much more technically demanding due to the technical challenges of removing the Si substrate without damaging the NW. In this manuscript, this second method is intended to benchmark the validity and robustness of the first one, with its main advantage being a more straightforward analysis. Even though it could be applied to assess certain production steps it is not intended as a systematic characterization technique according to its manufacturing complexity. Finally, the combination of the two approaches allows us to assess the robustness of the full stress analysis and to guarantee the reliability of the proposed model, the measurement methodology, and the etching process.

Conclusion

We presented two different methods for the characterization of stress profiles on Si NWs, which are applicable in the context of the manufacturing of semiconductor quantum devices.

In the first method, local heating was deliberately induced in the NW with the incident laser beam to modify its Raman spectrum. This enabled us to separate the NW and substrate peaks and extract the NW stress by decoupling it from the thermal effects. We obtained stress values of 0.17 ± 0.04 GPa and 0.34 ± 0.04 GPa for the Si NWs. The data showed no dependence on the applied laser power, pointing to the robustness of the method and the intrinsic nature of the obtained stress.

In the second method, we proposed an alternative route to directly access information from the Si NW, which involves removing the SiO_2 and the Si substrate beneath the NW. Comparing the stress profiles obtained experimentally with FEM simulations, we were able to extract the initial stress of the NWs for which we obtained the value of 0.21 ± 0.05 GPa. Both methods yield comparable stress values, validating the reliability of the whole method and showing that the fabrication process induces acceptable levels of stress in the NWs. Furthermore, the measured stress values correspond to minor elastic strains (0.1–0.2%) that would lift the heavy-hole/light-hole degeneracy and reduce band mixing. These modifications could favor hole-qubit operation while remaining well below mechanical damage thresholds.

This work thus establishes a methodology for nanoscale stress characterization, even under unfavourable conditions where the separation of stress and temperature contributions is not trivial, or the presence of the substrate prevents a clean measurement. The results confirm the suitability of the etching process and establish a reliable platform for a robust non-invasive characterization of Si NW-based qubits.

Materials and methods

Sample fabrication process

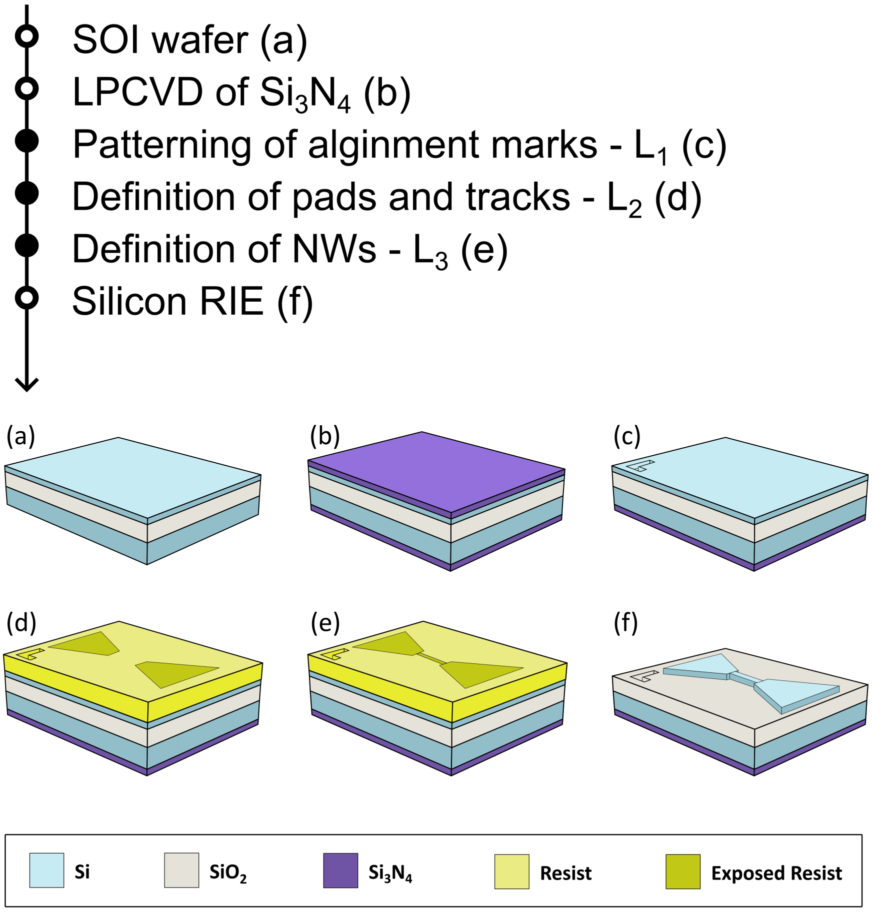

Figure 6: Fabrication flow of SiNWs using three lithographic levels (L_1–L_3). Front-side preparation: SOI wafer, LPCVD Si_3N_4 deposition, and alignment mark definition via optical lithography and DRIE. (d–e) Top-layer patterning with AR-N 7520.07 resist: large features defined by optical lithography (L_2), and SiNWs by electron beam lithography (L_3) on the same resist layer. (f) Pattern transfer by RIE and resist removal via oxygen plasma.

The fabrication process of Si NWs, illustrated in Figure 6, involves four lithographic steps (denoted as L_1–L_4). Starting from a silicon-on-insulator (SOI) wafer (Figure 6 (a)), a 50 nm layer of silicon nitride (Si_3N_4) is deposited via low-pressure chemical vapor deposition (LPCVD) as indicated in Figure 6 (b). The front-side Si_3N_4 is selectively removed, and alignment marks are defined using optical lithography (L_1), followed by deep reactive ion etching (DRIE) to etch 50 nm of silicon and 200 nm of buried oxide (Figure 6 (c)). The top-layer structures are patterned using AR-N 7520.07, a negative-tone mix-and-match resist from Allresist. This resist enables mix-and-match patterning: large features such as contact pads and tracks are defined by optical lithography (L_2) as indicated in Figure 6 (d), while high-resolution SiNWs are exposed using electron beam lithography (L_3) on a Raith 150 system (30 keV, $\sim$40 pA, 120 μC/cm^2) showed on Figure 6 (e). Both exposures are performed on the same resist layer without intermediate development. After development and a hard bake (1 min at 80 °C), the resist serves as an etch mask for pattern transfer into the top silicon layer using reactive ion etching (RIE) with SF_6/C_4F_8/Ar chemistry. The resist is subsequently removed via oxygen plasma stripping (Figure 6 (f)).

Free-standing Si NWs

For membrane definition and subsequent release of the NW through SiO_2 wet etching, a fourth lithography step (L_4) is performed on the wafer's backside, aligned to the front-side marks, as shown in Supplementary Data (Figure S2). An opening is etched on the backside Si_3N_4 layer (50 nm) by means of RIE, followed by resist removal using O_2 plasma. The remaining Si_3N_4 layer is used as a mask to completely wet-etch the bulk of the Si wafer (HF 5% dip to remove native silicon dioxide + KOH 40%) until the BOX layer is reached. Finally, the wafer is immersed in diluted HF, with the front side physically protected, to locally remove the SiO_2 membrane and release the NWs, as indicated in Figure 1 (c) and (d).

Experimental setup

The measurements were conducted using a HORIBA Soleil Raman Spectrometer. A laser emitting at a wavelength of 532 nm has been used. The emitted laser light is linearly polarized. Additionally, a typical Raman setup includes a microscope, a filter to eliminate Rayleigh radiation, and a spectrometer coupled with a CCD. A 100X objective with a numerical aperture (NA) of 0.9 was employed to focus the laser light on the sample while simultaneously collecting its Raman emission. The laser light is focused on a circular illumination area of approximately 720 nm, in accordance with the diffraction resolution-limit $\frac{1.22\lambda}{NA}$. To control the depth from which scattered light is collected and achieve confocality in the z-scan measurements, a pinhole of 10 μm is employed. For the horizontal scans along the free-standing NWs, a 200 μm pinhole was used to maximize the Raman signal. For all the measurements, a grating of 2400 lines/mm was used.

The laser power applied for intentional local heating of the Si NWs depends on the NW width and therefore varies across samples. In this study, values between 0.84 and 1.42 mW were employed, corresponding to power densities between 2.06×10^5 and 3.49×10^5 W/cm^2. In the case of free-standing NWs, the laser power was minimized to avoid heating effects while still providing an adequate signal-to-noise ratio. Accordingly, a power of 0.054 mW was used, corresponding to a power density of $I = 1.33 \times 10^4$ W/cm^2.

The acquisition time for the spectra varies depending on the type of measurement and the other parameters involved. However, before fitting the Lorentzian profile to the experimental spectra, the intensity values were normalized to 1 second acquisition time. The acquisition time ranged from 2 s for the free-standing Si NWs to 10 s for the unprocessed Si NWs.

To externally control the temperature of the samples, we used a Linkam THMS600 System.

Data availability

The data that support the findings of this study are openly available in the University of Valladolid repository (UVaDoc) at `https://uvadoc.uva.es/handle/10324/83047`.

Acknowledgements

The authors acknowledge the financial support from grants PID2021-126046OB-C21, PID2021-126046OB-C22, and PID2024-157972OA-C22 funded by MICIU/AEI/10.13039/501100011033 and by "ERDF/EU", and grant TED2021-130786B-I00 funded also by NextGenerationEU/PRTR. GGG acknowledges the financial support of Junta de Castilla y León through a predoctoral fellowship. This work was supported with funding from the Spanish government through the "María de Maeztu Unit of Excellence" accreditation CEX2023-001397-M. JLS acknowledges support from the grant RYC2023-043765-I, funded by MCIN/AEI/10.13039/501100011033 and FSE+ and the Trigger project INSPECTOR. J. Antoja-Lleonart - staff hired under the Generation D initiative, promoted by Red.es, an organization attached to the Ministry for Digital Transformation and the Civil Service, for the attraction and retention of talent through grants and training contracts, financed by the Recovery, Transformation and Resilience Plan through the European Union's Next Generation funds. The authors gratefully acknowledge Irene Mediavilla for her assistance with data acquisition and curation.

Author Contributions

Ginés González-Guirado: Methodology, Formal Analysis, Investigation, Data Curation, Writing - Original Draft, Visualization. **Vanessa Hinojosa-Chasiquiza:** Investigation, Validation. **Julián Anaya:** Methodology, Validation. **Jordi Antoja-Lleonart, Jordi Llobet:** Methodology, Investigation, Writing - Review & Editing. **Alberto del Moral** Investigation. **Albert Guerrero, Olga Muntada, Teresa Elenes-Cervantes:** Samples preparation. **Joan Bausells:** Conceptualization, Project administration. **Juan Jiménez:** Methodology, Writing - Review & Editing, Supervision. **Jorge Souto:** Methodology, Supervision, Project Administration, Funding Acquisition. **Francesc Pérez-Murano:** Conceptualization, Methodology, Writing - Review & Editing, Supervision, Project Administration, Funding Acquisition. **Jose Luis Pura:** Methodology, Formal Analysis, Investigation, Writing - Original Draft, Visualization, Supervision.

Conflict of Interest

The authors declare no conflict of interest.

References

[1] V. Lordi and J. M. Nichol, "Advances and opportunities in materials science for scalable quantum computing," MRS Bulletin, vol. 46, no. 7, pp. 589–595, Jul. 2021. [Online]. Available: https://link.springer.com/10.1557/s43577-021-00133-0

[2] A. G. Fowler, M. Mariantoni, J. M. Martinis, and A. N. Cleland, "Surface codes: Towards practical large-scale quantum computation," Physical Review A, vol. 86, no. 3, p. 032324, Sep. 2012. [Online]. Available: https://link.aps.org/doi/10.1103/PhysRevA.86.032324

[3] Q. Xu, J. P. Bonilla Ataides, C. A. Pattison, N. Raveendran, D. Bluvstein, J. Wurtz, B. Vasić, M. D. Lukin, L. Jiang, and H. Zhou, "Constant-overhead fault-tolerant quantum computation with reconfigurable atom arrays," Nature Physics, vol. 20, no. 7, pp. 1084–1090, Jul. 2024. [Online]. Available: https://www.nature.com/articles/s41567-024-02479-z

[4] A. Crippa, R. Ezzouch, A. Aprá, A. Amisse, R. Laviéville, L. Hutin, B. Bertrand, M. Vinet, M. Urdampilleta, T. Meunier, M. Sanquer, X. Jehl, R. Maurand, and S. De Franceschi, "Gate-reflectometry dispersive readout and coherent control of a spin qubit in silicon," Nature Communications, vol. 10, no. 1, p. 2776, Jul. 2019. [Online]. Available: https://www.nature.com/articles/s41467-019-10848-z

[5] J. T. Muhonen, J. P. Dehollain, A. Laucht, F. E. Hudson, R. Kalra, T. Sekiguchi, K. M. Itoh, D. N. Jamieson, J. C. McCallum, A. S. Dzurak, and A. Morello, "Storing quantum information for 30 seconds in a nanoelectronic device," Nature Nanotechnology, vol. 9, no. 12, pp. 986–991, Dec. 2014. [Online]. Available: https://www.nature.com/articles/nnano.2014.211

[6] M. Veldhorst, J. C. C. Hwang, C. H. Yang, A. W. Leenstra, B. De Ronde, J. P. Dehollain, J. T. Muhonen, F. E. Hudson, K. M. Itoh, A. Morello, and A. S. Dzurak, "An addressable quantum dot qubit with fault-tolerant control-fidelity," Nature Nanotechnology, vol. 9, no. 12, pp. 981–985, Dec. 2014. [Online]. Available: https://www.nature.com/articles/nnano.2014.216

[7] J. Yoneda, K. Takeda, T. Otsuka, T. Nakajima, M. R. Delbecq, G. Allison, T. Honda, T. Kodera, S. Oda, Y. Hoshi, N. Usami, K. M. Itoh, and S. Tarucha, "A quantum-dot spin qubit with coherence limited by charge noise and fidelity higher than 99.9%," Nature Nanotechnology, vol. 13, no. 2, pp. 102–106, Feb. 2018. [Online]. Available: https://www.nature.com/articles/s41565-017-0014-x

[8] S. Nadj-Perge, S. M. Frolov, E. P. A. M. Bakkers, and L. P. Kouwenhoven, "Spin–orbit qubit in a semiconductor nanowire," Nature, vol. 468, no. 7327, pp. 1084–1087, Dec. 2010. [Online]. Available: https://www.nature.com/articles/nature09682

[9] S. M. Frolov, S. R. Plissard, S. Nadj-Perge, L. P. Kouwenhoven, and E. P. Bakkers, "Quantum computing based on semiconductor nanowires,"

MRS Bulletin, vol. 38, no. 10, pp. 809–815, Oct. 2013. [Online]. Available: http://link.springer.com/10.1557/mrs.2013.205

[10] N. Piot, B. Brun, V. Schmitt, S. Zihlmann, V. P. Michal, A. Apra, J. C. Abadillo-Uriel, X. Jehl, B. Bertrand, H. Niebojewski, L. Hutin, M. Vinet, M. Urdampilleta, T. Meunier, Y.-M. Niquet, R. Maurand, and S. D. Franceschi, "A single hole spin with enhanced coherence in natural silicon," Nature Nanotechnology, vol. 17, no. 10, pp. 1072–1077, Oct. 2022. [Online]. Available: https://www.nature.com/articles/s41565-022-01196-z

[11] J. Llobet, E. Krali, C. Wang, J. Arbiol, M. E. Jones, F. Pérez-Murano, and Z. A. K. Durrani, "Resonant tunnelling features in a suspended silicon nanowire single-hole transistor," Applied Physics Letters, vol. 107, no. 22, p. 223501, Nov. 2015. [Online]. Available: https://pubs.aip.org/apl/article/107/22/223501/29111/Resonant-tunnelling-features-in-a-suspended

[12] J. Wang, E. Polizzi, A. Ghosh, S. Datta, and M. Lundstrom, "Theoretical investigation of surface roughness scattering in silicon nanowire transistors," Applied Physics Letters, vol. 87, no. 4, p. 043101, Jul. 2005. [Online]. Available: https://pubs.aip.org/apl/article/87/4/043101/331218/Theoretical-investigation-of-surface-roughness

[13] B. Martinez and Y.-M. Niquet, "Variability of Electron and Hole Spin Qubits Due to Interface Roughness and Charge Traps," Physical Review Applied, vol. 17, no. 2, p. 024022, Feb. 2022. [Online]. Available: https://link.aps.org/doi/10.1103/PhysRevApplied.17.024022

[14] J. D. Cifuentes, T. Tanttu, W. Gilbert, J. Y. Huang, E. Vahapoglu, R. C. C. Leon, S. Serrano, D. Otter, D. Dunmore, P. Y. Mai, F. Schlattner, M. Feng, K. Itoh, N. Abrosimov, H.-J. Pohl, M. Thewalt, A. Laucht, C. H. Yang, C. C. Escott, W. H. Lim, F. E. Hudson, R. Rahman, A. S. Dzurak, and A. Saraiva, "Bounds to electron spin qubit variability for scalable CMOS architectures," Nature Communications, vol. 15, no. 1, p. 4299, May 2024. [Online]. Available: https://www.nature.com/articles/s41467-024-48557-x

[15] S. Piscanec, M. Cantoro, A. C. Ferrari, J. A. Zapien, Y. Lifshitz, S. T. Lee, S. Hofmann, and J. Robertson, "Raman spectroscopy of silicon nanowires,"

Physical Review B, vol. 68, no. 24, p. 241312, Dec. 2003. [Online]. Available: https://link.aps.org/doi/10.1103/PhysRevB.68.241312

[16] Y. Chang, S. He, M. Sun, Y. Zhao, L. Ma, and W. Qiu, "Decoupling analysis of stress components on monocrystalline silicon using angle-resolved oblique backscattering Raman spectroscopy," Acta Mechanica Sinica, vol. 40, no. 4, p. 423418, Apr. 2024. [Online]. Available: https://link.springer.com/10.1007/s10409-023-23418-x

[17] G. S. Doerk, C. Carraro, and R. Maboudian, "Single Nanowire Thermal Conductivity Measurements by Raman Thermography," ACS Nano, vol. 4, no. 8, pp. 4908–4914, Aug. 2010. [Online]. Available: https://pubs.acs.org/doi/10.1021/nn1012429

[18] J. L. Pura, J. Anaya, J. Souto, A. C. Prieto, A. Rodríguez, T. Rodríguez, P. Periwal, T. Baron, and J. Jiménez, "Electromagnetic field enhancement effects in group IV semiconductor nanowires. A Raman spectroscopy approach," Journal of Applied Physics, vol. 123, no. 11, p. 114302, Mar. 2018. [Online]. Available: https://pubs.aip.org/jap/article/123/11/114302/155158/Electromagnetic-field-enhancement-effects-in-group

[19] J. L. Pura, J. Anaya, and J. Jiménez, "About the Interaction Between a Laser Beam and Group IV Nanowires: A Study of the Electromagnetic Field Enhancement in Homogeneous and Heterostructured Nanowires," physica status solidi (a), vol. 215, no. 19, p. 1800336, Oct. 2018. [Online]. Available: https://onlinelibrary.wiley.com/doi/10.1002/pssa.201800336

[20] L. Cao, J. S. White, J.-S. Park, J. A. Schuller, B. M. Clemens, and M. L. Brongersma, "Engineering light absorption in semiconductor nanowire devices," Nature Materials, vol. 8, no. 8, pp. 643–647, Aug. 2009. [Online]. Available: https://www.nature.com/articles/nmat2477

[21] F. J. Lopez, J. K. Hyun, U. Givan, I. S. Kim, A. L. Holsteen, and L. J. Lauhon, "Diameter and Polarization-Dependent Raman Scattering Intensities of Semiconductor Nanowires," Nano Letters, vol. 12, no. 5, pp. 2266–2271, May 2012. [Online]. Available: https://pubs.acs.org/doi/10.1021/nl204537d

[22] I. Zardo, S. Conesa-Boj, F. Peiro, J. R. Morante, J. Arbiol, E. Uccelli, G. Abstreiter, and A. Fontcuberta I Morral, "Raman spectroscopy of wurtzite and zinc-blende GaAs nanowires: Polarization dependence, selection rules, and strain effects,"

Physical Review B, vol. 80, no. 24, p. 245324, Dec. 2009. [Online]. Available: https://link.aps.org/doi/10.1103/PhysRevB.80.245324

[23] M. Möller, M. M. De Lima, A. Cantarero, L. C. O. Dacal, J. R. Madureira, F. Iikawa, T. Chiaramonte, and M. A. Cotta, "Polarized and resonant Raman spectroscopy on single InAs nanowires," Physical Review B, vol. 84, no. 8, p. 085318, Aug. 2011. [Online]. Available: https://link.aps.org/doi/10.1103/PhysRevB.84.085318

[24] A. Tarun, N. Hayazawa, M. V. Balois, S. Kawata, M. Reiche, and O. Moutanabbir, "Stress redistribution in individual ultrathin strained silicon nanowires: a high-resolution polarized Raman study," New Journal of Physics, vol. 15, no. 5, p. 053042, May 2013. [Online]. Available: https://iopscience.iop.org/article/10.1088/1367-2630/15/5/053042

[25] L. B. Spejo, J. L. Arrieta-Concha, M. V. Puydinger Dos Santos, A. D. Barros, K. K. Bourdelle, J. A. Diniz, and R. A. Minamisawa, "Non-linear Raman shift-stress behavior in top-down fabricated highly strained silicon nanowires," Journal of Applied Physics, vol. 128, no. 4, p. 045704, Jul. 2020. [Online]. Available: https://pubs.aip.org/jap/article/128/4/045704/563351/Non-linear-Raman-shift-stress-behavior-in-top-down

[26] M. Lorenzoni, J. Llobet, F. Gramazio, M. Sansa, J. Fraxedas, and F. Perez-Murano, "Evaluating the compressive stress generated during fabrication of Si doubly clamped nanobeams with AFM," Journal of Vacuum Science & Technology B, Nanotechnology and Microelectronics: Materials, Proc vol. 34, no. 6, p. 06KK02, Nov. 2016. [Online]. Available: https://pubs.aip.org/jvb/article/34/6/06KK02/103286/Evaluating-the-compressive-stress-generated-during

[27] S. D. Liles, F. Martins, D. S. Miserev, A. A. Kiselev, I. D. Thorvaldson, M. J. Rendell, I. K. Jin, F. E. Hudson, M. Veldhorst, K. M. Itoh, O. P. Sushkov, T. D. Ladd, A. S. Dzurak, and A. R. Hamilton, "Electrical control of the g tensor of the first hole in a silicon MOS quantum dot," Physical Review B, vol. 104, no. 23, p. 235303, Dec. 2021. [Online]. Available: https://link.aps.org/doi/10.1103/PhysRevB.104.235303

[28] N. Roisin, G. Brunin, G.-M. Rignanese, D. Flandre, J.-P. Raskin, and S. Poncé, "Phonon-limited mobility for electrons and holes in highly-strained silicon,"

npj Computational Materials, vol. 10, no. 1, p. 242, Oct. 2024. [Online]. Available: https://www.nature.com/articles/s41524-024-01425-0

[29] Y. Zhu, F. Xu, Q. Qin, W. Y. Fung, and W. Lu, "Mechanical Properties of Vapor-Liquid-Solid Synthesized Silicon Nanowires," Nano Letters, vol. 9, no. 11, pp. 3934–3939, Nov. 2009. [Online]. Available: https://pubs.acs.org/doi/10.1021/nl902132w

[30] D. Fan, H. Sigg, R. Spolenak, and Y. Ekinci, "Strain and thermal conductivity in ultrathin suspended silicon nanowires," Physical Review B, vol. 96, no. 11, pp. 1–11, 2017.

[31] J. W. Lee, M. H. Nam, J. H. Oh, J. W. Yang, W. C. Lee, H. K. Kim, M. R. Oh, and Y. H. Koh, "Effects of buried oxide stress on thin-film silicon-on-insulator metal–oxide–semiconductor field-effect transistor," Applied Physics Letters, vol. 72, no. 6, pp. 677–679, 2 1998. [Online]. Available: /aip/apl/article/72/6/677/68992/Effects-of-buried-oxide-stress-on-thin-film

[32] J. Anaya, A. Torres, A. Martín-Martín, J. Souto, J. Jiménez, A. Rodríguez, and T. Rodríguez, "Study of the temperature distribution in Si nanowires under microscopic laser beam excitation," Applied Physics A, vol. 113, no. 1, pp. 167–176, Oct. 2013. [Online]. Available: http://link.springer.com/10.1007/s00339-012-7509-y

[33] I. D. Wolf, "Micro-Raman spectroscopy to study local mechanical stress in silicon integrated circuits," Semiconductor Science and Technology, vol. 11, no. 2, pp. 139–154, Feb. 1996. [Online]. Available: https://iopscience.iop.org/article/10.1088/0268-1242/11/2/001

[34] X. Tang, N. Reckinger, G. Larrieu, E. Dubois, D. Flandre, J. P. Raskin, B. Nysten, A. M. Jonas, and V. Bayot, "Characterization of ultrathin SOI film and application to short channel MOSFETs," Nanotechnology, vol. 19, no. 16, p. 165703, 3 2008. [Online]. Available: https://iopscience.iop.org/article/10.1088/0957-4484/19/16/165703https://iopscience.iop.org/article/10.1088/0957-4484/19/16/165703/meta

[35] T. Kim and J. Lee, "Fabrication and characterization of silicon-on-insulator wafers," Micro and Nano Systems Letters 2023 11:1, vol. 11, no. 1, pp. 15–, 11 2023. [Online]. Available: https://link.springer.com/article/10.1186/s40486-023-00181-y

[36] J. Fréchette and C. Carraro, "Diameter-dependent modulation and polarization anisotropy in Raman scattering from individual nanowires," Physical Review B, vol. 74, no. 16, p. 161404, Oct. 2006. [Online]. Available: https://link.aps.org/doi/10.1103/PhysRevB.74.161404

[37] P. Martin, Z. Aksamija, E. Pop, and U. Ravaioli, "Impact of Phonon-Surface Roughness Scattering on Thermal Conductivity of Thin Si Nanowires," Physical Review Letters, vol. 102, no. 12, p. 125503, Mar. 2009. [Online]. Available: https://link.aps.org/doi/10.1103/PhysRevLett.102.125503

[38] D. Li, Y. Wu, P. Kim, L. Shi, P. Yang, and A. Majumdar, "Thermal conductivity of individual silicon nanowires," Applied Physics Letters, vol. 83, no. 14, pp. 2934–2936, Oct. 2003. [Online]. Available: https://pubs.aip.org/apl/article/83/14/2934/1059766/Thermal-conductivity-of-individual-silicon

[39] L. Liu and X. Chen, "Effect of surface roughness on thermal conductivity of silicon nanowires," Journal of Applied Physics, vol. 107, no. 3, p. 033501, Feb. 2010. [Online]. Available: https://pubs.aip.org/jap/article/107/3/033501/912609/Effect-of-surface-roughness-on-thermal

[40] Y. He and G. Galli, "Microscopic Origin of the Reduced Thermal Conductivity of Silicon Nanowires," Physical Review Letters, vol. 108, no. 21, p. 215901, May 2012. [Online]. Available: https://link.aps.org/doi/10.1103/PhysRevLett.108.215901

[41] J. Lim, K. Hippalgaonkar, S. C. Andrews, A. Majumdar, and P. Yang, "Quantifying Surface Roughness Effects on Phonon Transport in Silicon Nanowires," Nano Letters, vol. 12, no. 5, pp. 2475–2482, May 2012. [Online]. Available: https://pubs.acs.org/doi/10.1021/nl3005868

[42] H. H. Burke and I. P. Herman, "Temperature dependence of raman scattering in Ge_{1-x} Si_x alloys," Physical Review B, vol. 48, no. 20, pp. 15 016–15 024, Nov. 1993. [Online]. Available: https://link.aps.org/doi/10.1103/PhysRevB.48.15016

[43] X. Li, S. Jin, R. Zhang, Y. Gao, Z. Liu, Y. Yao, Y. Wang, X. Wang, Y. Zhang, and X. Tao, "The resolution and repeatability of stress measurement by Raman and EBSD in silicon," Vacuum, vol. 203, p. 111276, Sep. 2022. [Online]. Available: https://linkinghub.elsevier.com/retrieve/pii/S0042207X22004006

[44] F. Ureña, S. H. Olsen, and J.-P. Raskin, "Raman measurements of uniaxial strain in silicon nanostructures," Journal of Applied Physics, vol. 114, no. 14, p. 144507, Oct. 2013. [Online]. Available: https://pubs.aip.org/jap/article/114/14/144507/345042/Raman-measurements-of-uniaxial-strain-in-silicon

[45] F. Ureña-Begara, R. Vayrette, U. K. Bhaskar, and J.-P. Raskin, "Raman analysis of strain in p-type doped silicon nanostructures," Journal of Applied Physics, vol. 124, no. 9, p. 095102, Sep. 2018. [Online]. Available: https://pubs.aip.org/jap/article/124/9/095102/155705/Raman-analysis-of-strain-in-p-type-doped-silicon

[46] H. Richter, Z. Wang, and L. Ley, "The one phonon Raman spectrum in microcrystalline silicon," Solid State Communications, vol. 39, no. 5, pp. 625–629, Aug. 1981. [Online]. Available: https://linkinghub.elsevier.com/retrieve/pii/0038109881903379

[47] I. Campbell and P. Fauchet, "The effects of microcrystal size and shape on the one phonon Raman spectra of crystalline semiconductors," Solid State Communications, vol. 58, no. 10, pp. 739–741, Jun. 1986. [Online]. Available: https://linkinghub.elsevier.com/retrieve/pii/0038109886905132

[48] V. Magidson and R. Beserman, "Fano-type interference in the Raman spectrum of photoexcited Si," Physical Review B, vol. 66, no. 19, p. 195206, Nov. 2002. [Online]. Available: https://link.aps.org/doi/10.1103/PhysRevB.66.195206

[49] H. Zhang, J. Tersoff, S. Xu, H. Chen, Q. Zhang, K. Zhang, Y. Yang, C.-S. Lee, K.-N. Tu, J. Li, and Y. Lu, "Approaching the ideal elastic strain limit in silicon nanowires," Science Advances, vol. 2, no. 8, p. e1501382, Aug. 2016. [Online]. Available: https://www.science.org/doi/10.1126/sciadv.1501382

[50] M. Chu, Y. Sun, U. Aghoram, and S. E. Thompson, "Strain: A Solution for Higher Carrier Mobility in Nanoscale MOSFETs," Annual Review of Materials Research, vol. 39, no. 1, pp. 203–229, Aug. 2009. [Online]. Available: https://www.annualreviews.org/doi/10.1146/annurev-matsci-082908-145312

[51] B. Venitucci, L. Bourdet, D. Pouzada, and Y.-M. Niquet, "Electrical manipulation of semiconductor spin qubits within the g -matrix formalism," Physical Review B, vol. 98, no. 15, p. 155319, Oct. 2018. [Online]. Available: https://link.aps.org/doi/10.1103/PhysRevB.98.155319

[52] S. Zhang, Y. He, and P. Huang, "Acceptor-based qubit in silicon with tunable strain," Physical Review B, vol. 107, no. 15, p. 155301, Apr. 2023. [Online]. Available: https://link.aps.org/doi/10.1103/PhysRevB.107.155301

[53] J. Camassel, L. A. Falkovsky, and N. Planes, "Strain effect in silicon-on-insulator materials: Investigation with optical phonons," Physical Review B, vol. 63, no. 3, p. 035309, Dec. 2000. [Online]. Available: https://link.aps.org/doi/10.1103/PhysRevB.63.035309

[54] H. Yang, M. Liu, Y. Zhu, W. Wang, X. Qin, L. He, and K. Jiang, "Characterization of Residual Stress in SOI Wafers by Using MEMS Cantilever Beams," Micromachines, vol. 14, no. 8, p. 1510, Jul. 2023. [Online]. Available: https://www.mdpi.com/2072-666X/14/8/1510